Optical spectroscopy and optimal crystal growth of some Cr^{4+}-doped garnets

Optical spectroscopy and optimal crystal growth of some Cr⁴⁺-doped garnets

B Henderson, H G Gallagher, T P J Han† and M A Scott

Department of Physics and Applied Physics, University of Strathclyde, Glasgow G1 1XN, UK

E-mail: `t.han@strath.ac.uk`

Abstract. This paper describes the growth of single crystals of Cr^{4+}-doped $Y_3Ga_5O_{12}$ (YGG) and $Y_3Al_5O_{12}$ (YAG). Control of melt composition and post-growth annealing yields material that contains optimal concentrations of Cr^{4+} ions in distorted tetrahedral sites normally occupied by Ga^{3+} ions in YGG and Al^{3+} ions in YAG. Both Cr^{4+}-doped garnets exhibit strong visible and near-infrared absorption bands with peak cross sections of order 10^{-18}–10^{-19} cm² and emit into vibronically broadened but weakly allowed $^3B_2$ ($^3T_2$) $\to$ $^3B_1$ ($^3A_2$) transitions. Nonradiative decay is more efficient in YGG than in YAG as a consequence of the slightly reduced energy gap against radiative decay in the Ga-based garnet.

1. Introduction

The variety of laser applications that require tuning of the output wavelength has stimulated much research on novel optical materials and led to sundry new vibronic lasers. Tunable lasing at 300 K based on the $^4T_2 \to {}^4A_2$ emission band of Cr^{3+} ions was first reported for the alexandrite (Cr^{3+}:$BeAl_2O_4$) laser [1]. Many Cr^{3+}-doped lasers have been developed since with the Cr^{3+}-colquiriite lasers displaying exceptional near-infrared performance [2–5]. Attempts to extend the operation of Cr^{3+} lasers further into the infrared at 300 K with isomorphs of calcium gallogermanate ($Ca_3Ga_2Ge_4O_{12}$) foundered on efficient nonradiative decay [6, 7]. The laser operation of Cr-doped forsterite (Mg_2SiO_4) in the wavelength range 1160 nm to 1350 nm, at first identified with Cr^{3+} ions, was eventually assigned by magneto-optic studies to Cr^{4+} ions substituted for Si in tetrahedral sites [8–10]. Some early work on Czochralski-grown Cr:Nd:$Gd_3Sc_2Ga_3O_{12}$ (GSGG) revealed parasitic absorption at 1062 nm related to the presence of trace alkaline earth impurities [11]. Similar absorption in Cr-YAG was thought to pump laser operation over the wavelength range from 1350 nm to 1450 nm [12]. The active species was variously attributed to Cr^{3+} perturbed by O_2 ion vacancies, and to Cr^{2+} and/or Cr^{6+} ions in octahedral sites. Optical and electron spin resonance (ESR) spectroscopies confirmed that laser gain was provided by Cr^{4+} ions occupying distorted tetrahedral sites in the YAG structure [13–16]. Laser action has since been reported for various crystals containing Cr^{4+} or other $3d^2$ ions, including several garnets, Ca/Sr fluoroapatites, and other structurally related phosphates and vanadates [17–21]. The present study was undertaken to compare the energy level structures of Cr^{4+} ions in YAG and YGG and to optimize the Cr^{4+} content in these crystals.

---

† Corresponding author.

2. Symmetry and energy level structure

The oxide garnets are cubic with space group O_h^{10}. They can be represented structurally as $A_3B_2C_3O_{12}$ in which A, B and C are cation sites, *et seq.*, with approximately dodecahedral, octahedral and tetrahedral symmetries. In YAG the large disparity in the ionic radii of the Y^{3+} and Al^{3+} ions requires Y^{3+} to occupy the A sites and Al^{3+} to occupy both the B and C sites in maintaining chemical and structural order. In contrast, the similar sizes of Y^{3+} and Ga^{3+} ions in YGG allow the partial occupation of B sites by Y^{3+} ions. Compositional disorder in YGG causes inhomogeneous broadening of sharp line spectra. Normally, Cr^{3+} ions prefer to occupy octahedral B sites in YAG and YGG. However, the Cr^{4+} state can be induced by Czochralski growth in oxidizing atmospheres from melts co-doped with Cr and Ca oxides. The Ca^{2+} ions substitute on the A sites in partial charge-compensation for Cr^{4+} ions on tetrahedral C sites. An axially symmetric stretch of the $\langle 100 \rangle$-axes reduces the C-site symmetry from T_d to D_{2d}, introducing a deviation, α, from the bond angles of the perfect tetrahedron.

The crystal field Hamiltonian for $3d^2$ ions in tetrahedral symmetry contains even-parity terms that split energy levels and odd-parity terms that raise the Laporte selection rule against electric dipole transitions [22]. In pure tetrahedral symmetry spin triplet states, $^3A_2$, $^3T_2$ and $^3T_1$, in order of increasing energy, are derived from the lowest free ion level (^3F). A low lying ^1E level derived from the next highest level ($^1D_2$) is degenerate with $^3T_2$ and $^3T_1$ at different crystal field energies (10 Dq). Assuming that $^3A_2$ is the energy zero, ^1E varies rather little with Dq, whereas $^3T_2$ and $^3T_1$ are strong functions of Dq. Crystal field theory is not a quantitatively reliable predictor of state energies of tetrahedral molecular ions which feature mixed ionic–covalent bonding. In such cases the angular overlap model (AOM) of ligand field theory is better able to predict the ordering of levels. In this model the cubic ligand field is given by

$$E_{cub} = 10 \, Dq = (4/9)[4e_\pi - 3e_\sigma] \tag{1}$$

where e_π and e_σ are group overlap integrals for 3d-ligand antibonding orbitals [23]. The overall energy level structure is determined by the interplay of E_{cub} with the D_{2d} distortion, the inter-electron repulsion parameters B and C, the spin–orbit coupling and the electron–phonon interaction. The latter term broadens and adds stucture to the observed spectra, whereas other terms shift and split energy levels and determine the wavelength regimes of individual transitions. Using an AOM diagonalization of the full $3d^2$ basis set for Cr^{4+} in YAG, Riley *et al* [24] determined that the energy levels occur in the following order above the $^3B_1$ ($^3A_2$) ground state: $^3B_2$ ($^3T_2$), $^3A_2$ ($^3T_1$), $^1A_1$ (^1E), ^3E ($^3T_2$), $^1B_1$ (^1E) and ^3E ($^3T_1$), in accord with recent interpretations of the experimental spectra [24, 25]. The crystal field and spin–orbit-split levels of Cr^{4+} in D_{2d} symmetry and the selection rules for polarized optical spectra are shown in figure 1. A group theoretical formulation of the selection rules for Cr^{4+} in the C sites of YAG and YGG is given in Scott [26]. This information is useful in the comparisons of the absorption and luminescence spectra of Cr/Ca co-doped YAG and YGG that follows. Little detailed optical spectroscopy of Cr:Ca-YGG had been reported previously [17, 24, 26].

3. Experimental details

YAG and YGG crystals were grown from 5 N pure starting powders using a Crystalox Ltd radiofrequency induction furnace. Czochralski growth is ideal for such garnets because they melt congruently at the stoichiometric composition and their melts are chemically stable [11]. The starting charges were mixed from dried components in appropriate proportions and reacted
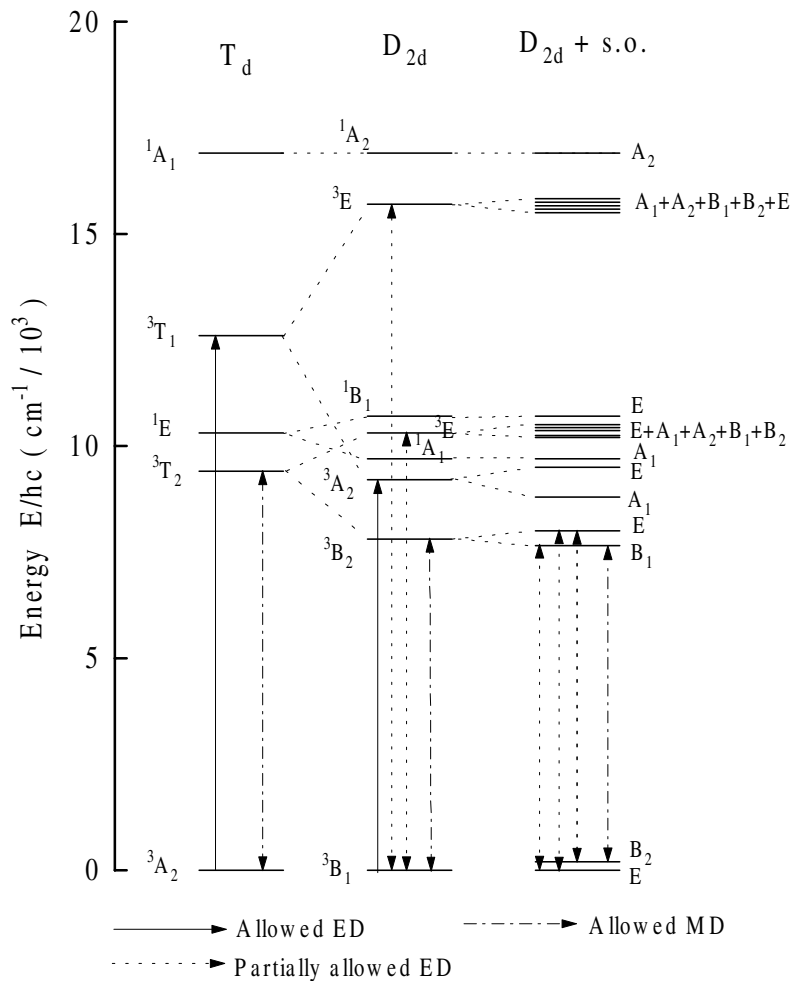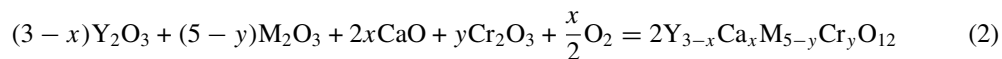
Figure 1. Electronic energy levels of Cr^{4+} ions in T_d symmetry appropriate to the C site in garnets, showing the splittings introduced by a D_{2d} distortion and spin–orbit coupling. Selection rules for some of the possible transitions are indicated.

in air at 1670 ± 50 K for 24 hours according to the equation,

$$(3 - x)Y_2O_3 + (5 - y)M_2O_3 + 2xCaO + yCr_2O_3 + \frac{x}{2}O_2 = 2Y_{3-x}Ca_xM_{5-y}Cr_yO_{12} \qquad (2)$$

where $M = Ga^{3+}$ or Al^{3+} and $x, y = 0.1$–4.0 at.% and it is assumed that Ca^{2+} replaces Y^{3+} and Cr^{3+} replaces Al^{3+} or Ga^{3+}. In view of their high melting temperatures YAG and YGG were contained in Ir crucibles that had internal dimensions of 35 mm $\times$ 35 mm diameter. The crucible, its lid and after-heater were supported in high purity zirconia and alumina ceramics. The formation of YGG from its constituent oxides by pre-reaction at low temperature minimizes the evaporation of Ga_2O_3 at the melt temperature ($\sim$2200 K). The furnace chamber operated in a static N_2 atmosphere containing a partial pressure of O_2 to minimize Ir oxidation and to suppress the reduction of melt oxides. In growing YAG only 1% O_2 in the furnace atmosphere prevented oxide decomposition. However, YGG needs higher O_2 contents to prevent the dissociation of Ga_2O_3 into Ga_2O and O_2 since the volatility of the sub-oxide can lead to evaporative weight

Table 1. Assignments of the optical absorption transitions at 300 K for Cr:Ca:YGG and Cr:Ca:YAG.

Peak energy (cm^{-1})		Optical	
YGG	YAG	Species	Transition
9860	9990	Cr^{4+}	$^3A_2 \rightarrow {}^3T_2$
15 118	14 705	Cr^{4+}	$^3A_2 \rightarrow {}^3T_1$
16 016	16 260	Cr^{4+}	$^3A_2 \rightarrow {}^3T_1$
16 129	16 611	Cr^{3+}	$^4A_2 \rightarrow {}^4T_2$
20 128	20 408	colour centres	—
22 321	22 371	Cr^{3+}	$^4A_2 \rightarrow {}^4T_1$
23 168	23 529	Cr^{6+}	$^1A_1 \rightarrow {}^1T_2$
28 213	27 778	Cr^{6+}	$^1A_1 \rightarrow {}^1T_2$

loss by as much as 0.025 g min^{-1}. The shape and dimensions of the growing boule were determined by computer-controlled feedback of the total weight of crucible plus charge in an automatic diameter control (ADC) unit. This system cannot distinguish between weight loss from the melt and weight gain by the boule. Hence, in growing YGG at low O$_2$ partial pressures, where weight loss and gain can be comparable, the ADC unit may increase the temperature of the melt and re-melt the boule. In consequence, YGG crystals were grown in an N$_2$/3% O$_2$ atmosphere to ensure satisfactory operation of the ADC unit. Even so Ga$_2$O$_3$ dissociation still caused vertical ridges on YGG boules at all N$_2$/O$_2$ compositions. The YGG and YAG boules were grown parallel to the $\langle 100 \rangle$ and $\langle 111 \rangle$ axes, respectively, using undoped or Cr^{3+}-doped seeds obtained from crystals prepared by spontaneous nucleation onto Ir wires. Growth rates of 4 mm hr^{-1} (YGG) and 2 mm hr^{-1} (YAG) were combined with rotation rates of 50–70 rpm. The higher pull rate for YGG further reduced Ga$_2$O evaporation at the growth interface, minimized the formation of compositionally induced optical inhomogeneities and reduced the tendency to spiral growth. Spiralling is well known in the Ga-based garnets, and can start after only $\sim$20% of the melt has crystallized. In this study more than 50% of the Ca:Cr:YGG and $\sim$80% of the Ca:Cr:YAG charges were recovered as single crystals.

Several Ca:Cr:YGG and Ca:Cr:YAG boules were grown from melts containing Ca/Cr ratios in the range 1:4 to 4:1 (1:1 to 5:1) in YAG (YGG). Optical absorption measurements were made on as-grown samples and on samples subsequently annealed at 1673 K in an N$_2$/20% O$_2$ atmosphere for 24 h, then for 60 h at 1373 K in pure O$_2$ and, finally, for 18 h in an N$_2$/2% H$_2$ atmosphere. Optical absorption spectra were measured at 300 K on 2 mm thick slices at each annealing stage. Detailed optical studies were carried out on polished crystal slices cut perpendicular to the growth axis from boules YAG2 and YGG4 (table 2) to typical dimensions 10 × 10 × 2 mm^3 and annealed in air at 1373 K for 24 h. (Laser rods should be cut parallel to the growth axis to avoid the effects of radial segregation of dopants.) The optical absorption spectra of YAG2 and YGG4 slices were measured at 300 K and 77 K in an AVIV-14DS dual beam spectrophotometer in the wavelength range 300–1250 nm. The polarization of the absorption coefficient was measured by inserting a Glan–Taylor prism before the crystal in the sample compartment. The sample temperature was reduced from 300 K to 77 K by attaching it to a Cu support rod in a liquid N$_2$ cryostat. Photoluminescence was excited at 15–20 K with either a Ti^{3+}-sapphire laser (700–820 nm) or a rhodamine 6G dye laser (580–620 nm) pumped by a 4 W Ar$^+$-ion laser. The laser light was focused onto the sample secured to the cold finger of a closed-cycle He refrigerator with separate windows for the access of the excitation and egress of the emission. The laser beam was mechanically chopped, the chopper providing a reference signal for phase-sensitive detection of the light emitted from the sample. The luminescence was focused on to the entrance to a 1 metre grating

Table 2. Summary of growth conditions used to grow the Cr:Ca garnet crystals.

Crystal	Melt dopant concentration (ions cm^{-3}) Cr:Ca^{2+}	Growth atmosphere	colour
YGG1	7×10^{18}:7×10^{18}	25% CO$_2$/N$_2$	green
YGG2	7×10^{18}:1.4×10^{19}	2.5% O$_2$	green/light brown
YGG3	1.5×10^{19}:3×10^{19}	2.5% O$_2$	dark brown/yellow
YGG4	7×10^{18}:3.5×10^{19}	2.5% O$_2$	dark brown/yellow
YGG5	7×10^{18}:2.8×10^{19}	2% O$_2$	light brown
YAG1	8×10^{19}:2×10^{19}	2% O$_2$	green
YAG2	8×10^{19}:1.6×10^{20}	2% O$_2$	dark brown
YAG3	7×10^{18}:2.8×10^{19}	2% O$_2$	light brown

monochromator, dispersed by a grating and measured at the exit slit by a Ge photodetector and dual phase, lock-in amplifier. The electrical signal was processed by a differential amplifier and microcomputer.

4. Experimental results and discussion

4.1. Crystal growth

YAG boules were grown on $\langle 111 \rangle$ axes with an hexagonal cross-section and facets parallel to the $\{211\}$ and $\{110\}$ planes. Faceted growth causes inhomogeneous dopant segregation due to different segregation rates in the on- and off-facet regions. A three-fold, dark brown pattern is evident around a central core in sections cut perpendicular to the growth direction. YGG crystals grown along $\langle 100 \rangle$ directions showed less well developed $\{110\}$ facets and a fourfold pattern of colouration. These growth patterns are due to the radial segregation of impurities. In both materials the brown staining is due to preferential segregation of Ca^{2+} ions onto facet planes, where the Cr-dopant adopts the higher oxidation state of Cr^{4+} or Cr^{6+} in C sites to compensate for the charge deficiency of Ca^{2+} ions occupying the A sites. Normally faceting proceeds from growth at convex liquid–solid interfaces. Planar interfaces can be maintained during YGG growth by adjusting the axial and radial temperature gradients, and the rotation and pull rates thereby eliminating the different on–off facet segregation rates. Convex liquid–solid interfaces persist during YAG growth and there is always some non-uniformity in the distribution of dopants.

All YGG and YAG boules showed colour gradations along their length. Some also showed colour differences (table 2): the colours of as-grown crystals, reflecting the increasing Cr^{4+} content, changed from green to yellow to brown at larger Ca/Cr ratios and total Cr concentrations in the melt. Generally, the first material to crystallize (at the top of the boule) is a distinctive green colour, becoming increasingly brown towards the bottom, qualitatively showing that Ca^{2+} and Cr dopants segregate at different ends of the boule. Large Ca^{2+} levels cause Cr to adopt the Cr^{4+} state responsible for the brown colour. The axial segregation coefficient, k_{eff}, was determined from the normal freeze equation for perfect mixing,

$$C_s = C_0 k_{eff} (1-g)^{(k_{eff}-1)} \tag{3}$$

where C_0 and C_s are the dopant concentrations in the starting melt and solid, respectively, and g is the melt fraction that has crystallized [27]. A dopant-sensitive property of the crystal is measured at positions between tops and bottoms of the boules to permit k_{eff} to be estimated.

Values of k_{eff} for Cr^{3+} were measured for singly-doped boules from the peak absorption coefficient in the $^4A_2 \rightarrow\ ^4T_2$ band using sections cut from near the tops ($g = 0$) and bottoms ($g = 0.5$–0.8) of boules. For the co-doped boules the Ca^{2+} and total Cr contents were measured by x-ray fluorescence spectroscopy. The values of k_{eff} estimated for Cr^{3+} in YAG and YGG were 3.0 ± 0.1 and 3.2 ± 0.1, respectively. The value of k_{eff} for Ca^{2+} in both garnets was 0.1 ± 0.02, and independent of the Ca/Cr ratio over the range 1:1 to 5:1. These values of k_{eff} confirm that Ca^{2+} segregates at the top of the boule and Cr at the bottom. To achieve a fairly uniform distribution of Cr^{4+} requires a significant Ca excess to be present in the melt to compensate for the different concentration gradients of Ca^{2+} and Cr dopants.along the boule. Optimal results were obtained with Ca/Cr ratios greater than 3.5:1 i.e. boules YAG3, YGG4 and YGG5, as specified in table 2.

4.2. Optical characterization and Cr^{4+} optimization

The optical absorption spectra of YAG2 and YGG4 crystals measured in the infrared (900–1250 nm) and visible (300–900 nm) regions, respectively, at 300 K are shown in figures 2 and 3. The infrared bands in figure 2 are relatively weak, the absorption coefficient for as-grown samples being $<0.5\,cm^{-1}$ in YGG and $<1.2\,cm^{-1}$ in YAG, at all wavelengths. The band widths are slightly larger in YGG than in YAG due to disorder in the Ga garnet. The most intense band, which occurs at 1014 (1029) nm in YAG (YGG), is due to the $^3B_1$ ($^3A_2$) $\rightarrow\ ^3A_2$ ($^3T_1$) transition. A weaker infrared band at 1115 nm (1124 nm) in YAG (YGG) is assigned to the weakly allowed $^3B_1$ ($^3A_2$) $\rightarrow\ ^3B_2$ ($^3T_2$). Annealing in $N_2 + 2\%\ O_2$ atmospheres at 1673 K for 24 h introduces new infrared bands with peaks at 840 (930), 1020 (1050) and 1115 (1125) nm in YAG (YGG). Further annealing in pure O_2 at 1373 K for $\sim$60 h enhanced these bands further but only by $\sim$20%. Visible absorption bands in as-grown material, figures 2 and 3, occur at 430 (440) and 600 (620) nm in YAG (YGG) and are identified with the $^4A_2 \rightarrow\ ^4T_1$ and $^4A_2 \rightarrow\ ^4T_2$ transitions, respectively, of Cr^{3+} ions in octahedral B sites. These bands cause the distinctive green colour of the as-grown boules or part boules (table 2). Concomitant changes in the visible spectra following the oxidising anneal include reduced absorption in the Cr^{3+}
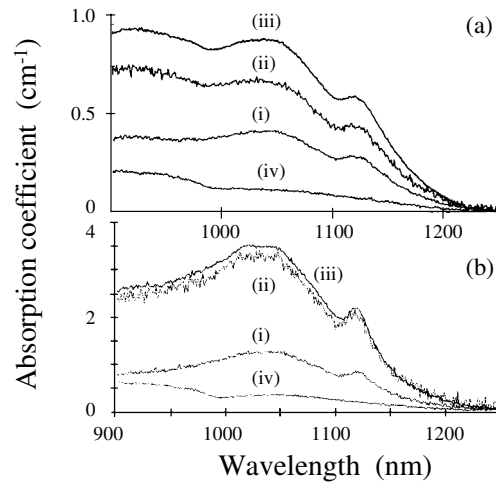

Figure 2. 300 K near-infrared optical absorption spectra of (a) YGG4 and (b) YAG2 crystals after various heat treatments: (i) as grown; (ii) 24 h at 1673 K in 20% O_2; (iii) 60 h at 1373 K in 100% O_2; (iv) 18 h at 1373 K in 2% H_2.
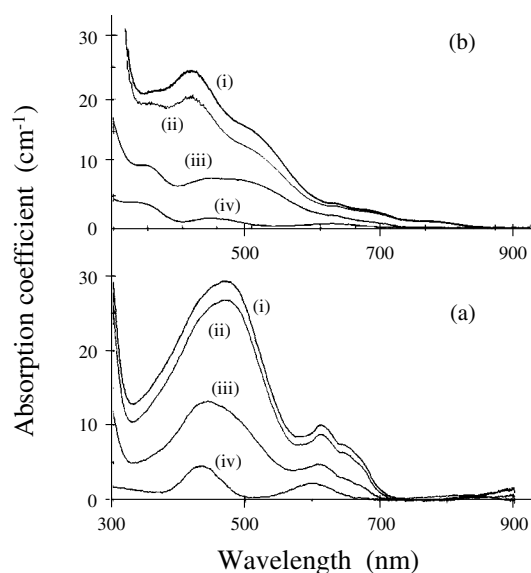
Figure 3. 300 K visible region optical absorption spectra of (a) YAG2 and (b) YGG4 crystals after various heat treatments: (i) as grown; (ii) 24 h at 1673 K in 20% O$_2$; (iii) 60 h at 1373 K in 100% O$_2$; (iv) 18 h at 1373 K in 2% H$_2$.

bands and new peaks between 600 and 700 (650–800) nm in YAG (YGG) assigned to Cr^{4+} ions in tetrahedral C sites. Other bands near 300 (325) and 425 (435) nm are attributed to the $^1A_1 \rightarrow \, ^1T_2$ electric dipole transition of tetrahedrally coordinated Cr^{6+} ions. The 425 (435) nm bands are overlapped by intense peaks near 500 nm, which have been assigned to charged vacancy centres that partially compensate for Ca^{2+} ions substituting for Y^{3+} on the C sites. These spectra are typical of co-doped materials in which it is difficult to resolve overlapping absorption bands except by careful comparisons of as-grown and annealed samples. There is some advantage to measuring the spectra at low temperature where the overlapping bands are slightly narrower.

Annealing the samples in oxidizing atmospheres at 1673 K for 24 h produces significant changes in the absorption spectra only when the Ca/Cr ratio exceeds 2:1; otherwise the visible Cr^{3+} absorption bands are almost unaffected. Annealing of the more strongly doped samples, YAG2 and 3 and YGG3 and 5 (table 2), where Ca/Cr > 2, results in the brown colour suffusing throughout the samples. Examination of figures 2 and 3 show that the visible and near-infrared absorption bands become more intense by a factor of 10 or so. There are also marked increases in the O^{2-} vacancy band at 500 nm. Further annealing at 1373 K in pure O$_2$ yields smaller changes in the intensities of these spectra resulting from smaller changes in the concentrations of associated centres. These changes are almost completely reversed by annealing for 18 h at 1373 K in a reducing atmosphere, as figures 2 and 3 also show.

On grounds of ionic size it is probable that Ca^{2+} ions substitute for Y^{3+} ions on dodecahedral A sites. Some of the Cr impurity can adopt the Cr^{4+} and Cr^{6+} states on tetrahedral C sites but in as-grown boules octahedral B-site occupation by Cr^{3+} is dominant. Given the overlapping spectra the mechanisms by which the Cr dopant changes valence state and lattice site have not been identified, especially in view of the uncertain charge on the O^{2-} vacancy centres. However, optimization of the Cr^{4+} concentration on the tetrahedral sites was achieved.

Co-doping to Ca/Cr ratios greater than 3.5:1 yields fairly uniform Cr^{4+} content along the lengths of boules. An oxidizing anneal then enhances the absorption coefficient at 1050 nm by a factor of two to three. Although the maximum effect in figures 2 and 3 is introduced by a two-stage anneal the same result can be effected by a long, single anneal ($\sim$48 h) at 1673 K in a $N_2/2\%$ O_2 atmosphere.

4.3. Energy levels of Cr^{4+} in YGG and YAG

The selection rules for $3d^2$ ions in T_d symmetry, figure 1, show that the $^3A_2 \rightarrow {}^3T_1$ transitions are allowed electric dipole transitions. Other low lying transitions, $^3A_2 \rightarrow {}^3T_2$ and ^1E are forbidden in the electric dipole approximation. However, the tetragonal distortion and spin–orbit coupling introduce splittings of all the levels and partially raise the selection rule against the normally forbidden components of the $^3A_2 \leftrightarrow {}^3T_2$ transitions. The many spectral features revealed in figures 2 and 3 suggest that the interpretation of spectra requires that account be taken of these splittings. The polarized selection rules are deduced from group theory by determining which function spaces in the character tables transform as the product $\Gamma_a \times \Gamma_b$ of the $\Gamma_a \leftrightarrow \Gamma_b$ transition. It follows from figures 2 and 3 that the very strong absorption bands in the visible region derive from the $^3A_2 \rightarrow {}^3T_1$ transition in T_d symmetry and those in the near infrared from $^3A_2 \rightarrow {}^3T_2$ transitions.

   A ligand field–AOM calculation for Cr^{4+}-YAG shows that the D_{2d} distortion splits the $^3T_1$ state into $^3A_2$ and ^3E levels separated by $\sim$6500 cm^{-1}, of which $^3A_2$ is lowest [24]. The $^3B_1$ ($^3A_2$) $\rightarrow {}^3E$ ($^3T_1$) transition occurs in the visible region as a structured band with peak at 640 nm in YAG and at 670 nm in YGG, the structure being due to the combined effects of spin–orbit and electron–phonon couplings. (The parent states in tetrahedral sites are indicated parenthetically.) There is simpler structure on the $^3B_1$ ($^3A_2$) $\rightarrow {}^3A_2$ ($^3T_1$) absorption band, which occurs with large cross section $\sigma_a = 5.17 \times 10^{-18}$ cm^2, measured at 1062 nm [25]. Since in figures 2 and 3 the corresponding absorption coefficient at this wavelength for as-grown samples is only $\alpha = 0.5$–1.0 cm^{-1}, and since also $\alpha = \sigma_a N$, only $\sim N = 1.0$–2.0×10^{17} cm^{-3} active ions result from a melt doping with 7×10^{19} Cr ions cm^{-3}. That only 1–2% of Cr dopant ions appear as Cr^{4+}, increased to 3–4% in crystals by a suitable oxidizing anneal shows that Cr^{4+} in tetrahedral sites is the minority state in Ca/Cr co-doped YAG and YGG crystals.

   The $^3B_1$ ($^3A_2$) $\rightarrow {}^3A_2$ ($^3T_1$) absorption shown in figure 4 has resolved vibronic structure at low temperatures, $<$100 K, for both Cr^{4+}:YAG and YGG. The sharp zero-phonon and one-phonon lines observed at 1114 nm (8977 cm^{-1}) and 1077 nm (9281 cm^{-1}) in Cr^{4+}-YAG, are shifted to 1123 nm (8919 cm^{-1}) and 1093 nm (9140 cm^{-1}) in Cr^{4+}-YGG. The shift to longer wavelengths of spectra in YGG is due to the slightly weaker crystal field compared with YAG. Note that the structure in figure 4 is rather broader for YGG than YAG: the halfwidths of the 1093 nm (YGG) and 1114 nm (YAG) zero-phonon lines, respectively, 130 and 36 cm^{-1}, are clear examples of inhomogeneous broadening by compositional disorder on the A and B sublattices in the YGG host, where it occurs due to the similar ionic radii of the Ga^{3+} and Y^{3+} ions [28]. The greater intensity of the vibronic sidebands relative to the zero-phonon lines in figure 4 indicates strong electron–phonon coupling, in which lattice modes involving the (AlO_4) molecular ions feature strongly [22, 29].

   The assignment of the 1114 nm zero-phonon line in the Cr^{4+}-YAG spectrum, figure 4, and the associated vibronic sideband was established by polarized absorption/luminescence and piezospectroscopic studies that removed a number of the earlier inconsistencies in the interpretation of the optical spectra of the co-doped Ca/Cr YAG material [25]. Complicit in the puzzling ambiguities of spectral and electronic assignments were the multiple charge states
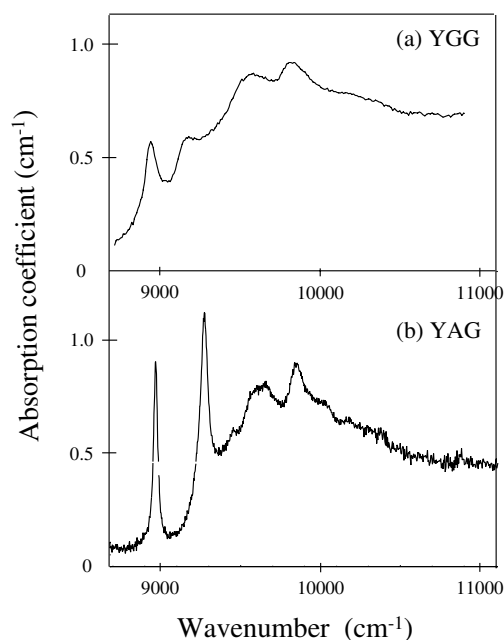
Figure 4. The vibronic shape of the $^3B_1$ ($^3A_2$) → $^3A_2$ ($^3T_1$) absorption band measured at 77 K for samples YGG2 and YAG2 annealed in an N_2/20% O_2 atmosphere at 1673 K for 24 h.

and site symmetries of Cr dopants and lattice defects that determine the detailed charge balance in co-doped garnets. The nature of some initial uncertainty in ordering the excited states of Cr^{4+} in YAG, and by implication YGG, is evident in figure 5 which compares the lowest energy absorption and luminescence spectra of Cr^{4+} ions in YAG and YGG. Irrespective of whether luminescence is excited in the visible (600–700 nm) or near infrared (900–1100 nm) this is the only spectrum observed. In both hosts the spectra are dominated by the vibronic sidebands with peaks at 500 nm and 1380 nm in YGG and YAG, respectively with halfwidths of 290 nm and 160 nm. There is an energy difference of more than 1000 cm^{-1} between the zero-phonon lines in absorption and emission, which cannot eventuate for vibronic transitions involving the same pair of electronic levels since then the zero-phonon lines would be coincident. The greater widths of the zero-phonon line and sideband in the Cr^{4+}-YGG reflect the extensive disorder that persists in Ga-based garnets [27].

Tissue *et al* [30] identified the emission spectrum of Cr^{4+}-YAG with $^1A_1$ (^1E) → $^3B_1$ ($^3A_2$) transitions, a conclusion at variance with the emission lineshapes and lifetimes. The zero-phonon emission lines in YAG and YGG are much weaker than their sidebands. For $^1A_1$ → $^3B_1$ transitions the zero-phonon line should be much stronger than the sideband, as it is for this transition in Mn^{5+}:Sr$_{10}$F$_2$(VO$_4$)$_6$ and for similar intra-configurational transitions in a variety of crystals. The decay patterns were measured at 300 K and 15 K after pulsed excitation at 670 nm with a DCM dye laser, at which wavelength there is strong absorption, and monitored at 1450 nm for Cr^{4+}-YGG and 1300 nm for Cr^{4+}-YGG. The luminescence decay times of Cr^{4+} ions at 15 K were 30.6 μs in YAG and 20.0 μs in YGG, shortening at 300 K to 4.1 and 2.4 μs, respectively. The lifetimes of spin-forbidden transitions should be of the order of several milliseconds duration rather than microseconds. The shorter luminescence decay times measured at 300 K are attributed to nonradiative processes, that also reduce the emission intensity with increasing temperature [17]. In consequence, this near-infrared
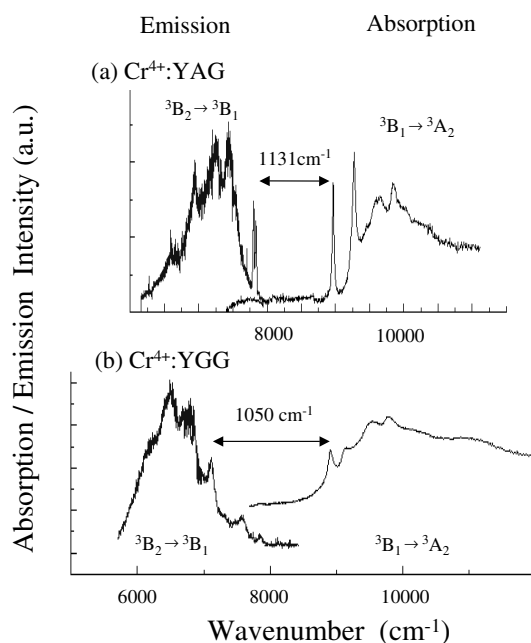
Figure 5. Comparing the near-infrared absorption and emission bands at 77 K and 15 K, respectively, of samples YGG2 and YAG1 heat treated as for figure 4.

emission is assigned to the $^3B_2$ ($^3T_2$) $\rightarrow$ $^3B_1$ ($^3A_2$) transition of Cr^{4+} ions in D_{2d} symmetry, as has been confirmed in the case of Cr^{4+}-doped YAG by polarized absorption/emission [25], magnetic circular dichroism and ligand field theory [24]. Accordingly, the ~1000 cm^{-1} separation between the zero-phonon lines in figure 5 measures the energy difference between the $^3B_2$ ($^3T_2$) and $^3A_2$ ($^3T_1$) excited states. Although the $^3B_2$ ($^3T_2$) $\rightarrow$ $^3B_1$ ($^3A_2$) transition originates from a forbidden electric dipole transition, the D_{2d} crystal field in concert with spin–orbit coupling induces a significant emission cross section. Indeed the radiative lifetimes measured at low temperature are consistent with $\sigma_e = 4.3 \times 10^{19}$ cm^2 for Cr^{4+}:YGG and 3.3×10^{-19} cm^2 for Cr^{4+}:YAG, in accord with values for other Cr^{4+}-doped garnets [17].

Close examination of figure 5 reveals there to be weak but finite absorption and emission signals between 1120 nm and 1330 nm for both materials. Indeed the zero-phonon absorption line at 1280 nm (1310 nm) in YAG (YGG) can be resolved at higher gain, in company with their sidebands, and by emission excitation and MCD spectroscopies [24, 25]. As can be seen in figure 1 both $^3B_1$ ($^3A_2$) ground state and $^3B_2$ ($^3T_2$) excited states are split by spin–orbit interaction. The E–B$_2$ ground state splitting measured by MCD is 1.2 cm^{-1} [24]. The measured E–B$_1$ splitting of $^3B_2$ ($^3T_2$) is ~30 cm^{-1}, in agreement with MCD measurements and the AOM prediction [24]. The disorder-induced broadening of the YGG spectra ensures that this splitting is not resolved. Other weak spectra in this region include the $^3B_1$ ($^3A_2$) $\rightarrow$ $^1A_1$ (^1E) line from the $^3A_2 \rightarrow$ ^1E transition, recognized by the effects of hydrostatic pressure on the near-infrared spectra of Cr^{4+}:YAG. Weak absorption and emission spectra from Cr^{4+} species in weaker crystal field sites associated with charge compensating ions or defects are observed [24, 25], but these were not studied. A summary of the assigned optical transitions at 300 K is presented in table 1.

5. Concluding remarks

The absorption and luminescence spectra of Cr^{4+} ions in the YGG and YAG hosts are very similar, the red-shifts of YGG relative to YAG being due to the weaker crystal field and greater spectral width reflecting the Y^{3+}/Ga^{3+} substitutional disorder. The spectral location, splittings, bandshapes and decay patterns are identical, after allowance for the effects of different unit cell size and chemical make-up. The assignments of the various spectra for Cr^{4+}:YGG can be based on those for Cr^{4+}:YAG now that the earlier ambiguities have been resolved [24, 25]. In consequence, the values of the cubic ligand field, $10\,Dq$ (equation (1)), and Racah parameters B and C, are almost identical, *viz.* for YAG (YGG) $10\,Dq = 10\,100$ cm (9950) cm^{-1}, $B = 460$ (430) cm^{-1}, and $C/B = 8.20$, similar to the values obtained from fitting the observed spectra to a ligand field calculation [24]. Consistent with these values are the surprisingly large splittings of the excited $^3T_1$ (6500 cm^{-1}), $^3T_2$ (2500 cm^{-1}) and ^1E (1500 cm^{-1}) states that make for satisfactory interpretation in terms of conventional crystal field theory.

The observed spectra are strongly temperature dependent, increasing temperature broadening and weakening the zero-phonon lines and their sidebands until at room temperature only vestiges of the vibronic structure remain. In general, the near-infrared absorption and luminescence bands derived from the forbidden $^3A_2 \leftrightarrow {}^3T_2$ transitions of ions in T_d-symmetry only have significant cross sections only because they are induced by the combined effects of the tetragonal distortion and spin–orbit interaction. The strength and width of these infrared spectra excite interest for applications in tunable solid state lasers. However given the complex charge compensating processes in co-doped crystals some attention has to be given to optimizing the amount of Cr^{4+} in the tetrahedral C site. This was achieved by the growth and post-growth annealing of crystals having appropriate Ca/Cr ratios in slightly oxidizing atmospheres. The broad absorptions from 600 to 700 and 900 to 1100 offer potential of gain media for efficient diode pumped solid state lasers with applications in near-infrared spectroscopy, ultrafast fibre optic test systems, remote sensing and in medicine. In this context a range of very compact, high repetition rate, all-solid-state Cr^{4+} lasers have been developed that are diode pumped via Nd-YVO$_4$ lasers or Yb-glass fibre amplifiers [31, 32]. Since the garnets have high damage thresholds and excellent thermal and chemical stability they also have potential for application in passive *Q*-switched device four-level saturable absorbers at Nd-YAG and Cr-LiSAF wavelengths. The broadband absorption of visible and near-infrared radiation also provides an efficient sensitization medium for rare earth ions such as Yb^{3+} and Er^{3+}.

Acknowledgments

References

[1] Walling J C, Peterson O G, Jenssen H P, Morris R C and O'Dell W 1980 *J. Quantum. Electron.* **16** 1302
[2] Moulton P 1985 *Laser Handbook* ed M Bass and M L Stitch (Amsterdam: Elsevier) pp 203–50
[3] Caird J A and Payne S A 1991 *Handbook of Laser Science and Technology* ed M J Weber (Boca Raton, FL: CRC Press) suppl 1, p 3
[4] Struve B and Huber G 1985 *Appl. Phys.* B **57** 45
[5] Payne S A, Chase L L, Newkirk H W, Smith L K and Krupke W F 1988 *IEEE Quantum Electron.* **24** 2243
[6] Kaminskii A A, Butashin A V, Demidovich A A, Mill B V and Shkadarevich A P 1989 *Phys. Status Solidi* a **112** 197

[7]   Macfarlane P I, Han T P J, Henderson B and Kaminskii A A 1994 *Opt. Mater.* **3** 15
       See also Lai S T, Chai B H T, Long M and Shinn M D 1922 *IEEE Quantum Electron.* **24** 1922
[8]   Petricevic V, Gayen S K and Alfano R R 1988 *Appl. Opt.* **27** 4162
[9]   Moncorgé R, Simkin D J, Cormier G and Capobianco J A 1989 *OSA Proc. Tunable Solid State Lasers* **8** 93
[10] Hoffmann K R, Casas-Gonzalez J, Jacobsen S M and Yen W M 1991 *Phys. Rev.* B **44** 12 589
[11] Fratello V J, Brandle C D and Valentino A J 1987 *J. Cryst. Growth* **85** 229
[12] Krutova L I, Kulagin N A, Sandulenko V A and Sandulenko A V 1989 *Sov. Phys.–Solid State* **31** 1193
[13] Hoffmann K R, Jacobsen S M, Casas-Gonzalez J and Yen W M 1991 *OSA Proc. Adv. Solid State Lasers* **10** 44
[14] Angert N B, Borodin N I, Garmash V M, Zhitnyuk V A, Okrimchuk A G, Ho Siyuchenko O G and Shestakov A V
          1988 *Sov. J. Quantum. Electron.* **18** 73
[15] Hoffmann K R, Homerich U, Jacobsen S M and Yen W M 1992 *J. Lumin.* **52** 277
[16] Kuck S, Petermann K and Huber G 1991 *OSA Proc. Adv. Solid State Lasers* **10** 92
[17] Kuck S, Petermann K, Pohlmann U and Huber G 1995 *Phys. Rev.* B **51** 17 323
[18] Oetliker U, Herren M, Gudel H U, Kesper U, Albrecht C and Reiner D 1994 *J Chem. Phys.* **100** 8696
[19] Merkle L D, Pinto A, Verdun H R and McIntosh B 1982 *Appl. Phys. Lett.* **61** 2386
[20] Merkle L D, Guyot Y and Chai B H T 1995 *J. Appl. Phys.* **77** 474
[21] Herren M, Gudel H U, Albrecht C and Reinen D 1991 *Chem. Phys. Lett.* **183** 98
[22] Henderson B and Imbusch G F 1990 *Optical Spectroscopy of Inorganic Solids* (Oxford: Clarendon) ch 4
[23] Gerloch M 1990 *Magnetism and Ligand Field Analysis* (Cambridge: Cambridge University Press)
[24] Riley M J, Krause E R, Manson N B and Henderson B 1998 *Phys. Rev.* B **59** 1850
[25] Eilers H, Homerich U, Jacobsen S M, Yen W M, Hoffmann K R and Jia W 1994 *Phys. Rev.* B **49** 15 505
[26] Scott M A 1995 *PhD Thesis* University of Strathclyde
[27] Scheil E 1942 *Z. Metallk.* **34** 70
[28] Marshall A, Henderson B, O'Donnell K P, Yamaga M and Cockayne B 1990 *Appl. Phys.* A **50** 565
[29] Hurrell J P, Porto S P S, Chang I F, Mitraand S S and Bauman R P 1968 *Phys. Rev.* **173** 851
[30] Tissue B M, Jia W and Yen W M 1991 *J. Appl. Phys.* **70** 3775
[31] Tong Y P, French P M W, Taylor J R and Fujimoto J O 1997 *Opt. Commun.* **136** 235
[32] Mellish R, Chernikov S V, French P M W and Taylor J R 1998 *Electron. Lett.* **34** 552